Thermal modeling of industrial-scale vanadium redox flow batteries in high-current operations

Andrea Trovò, Alberto Saccardo, Monica Giomo, Massimo Guarnieri

Department of Industrial Engineering – University of Padua

Interdepartmental Centre Giorgio Levi Cases for Energy Economics and Technology, University of Padua, Padova, Italy

Abstract A cell-resolved model that simulates the dynamic thermal behavior of a Vanadium Redox Flow Battery during charge and discharge is presented. It takes into account, at a cell level, the reversible entropic heat of the electrochemical reactions, irreversible heat due to overpotentials, self-discharge reactions due to ion crossover, and shunt current losses. The model accounts for the heat transfer between cells and toward the environment, the pump hydraulic losses and the heat transfer of piping and tanks. It provides the electrolyte temperature in each cell, at the stack inlet and outlet, along the piping and in the tanks. Validation has been carried out against the charge/discharge measurements from a 9kW/27kWh VRFB test facility. The model has been applied to study a VRFB with the same stack but a much larger capacity, operating at ±400 A for 8 h, in order to identify critical thermal conditions which may occur in next-generation industrial VRFB stacks capable to operating at high current density. The most critical condition has been found at the end a long discharge, when temperatures above 50°C appeared, possibly resulting in VO_2^+ precipitation and battery faults. These results call for heat exchangers tailored to assist high-power VRFB systems.

Key words: Vanadium redox flow battery, thermal analyses, reversible entropic heat, irreversible heat, Joule losses, heat transfer.

1 Introduction

Energy storage with Vanadium Redox Flow Batteries (VRFBs) is expected to play a major role in the future energy scenarios powered by carbon-free intermittent renewable energy sources, due to main benefits of VRFBs, including power/energy decoupling, long cycle life, low environmental impact and operational flexibility [1], [2], [3], [4]. In addition, VRFBs can cover many different services in future smart grids, e.g. load leveling, peak shaving, uninterruptible power supplies (UPS), emergency backup [5] and energy buffer for electric vehicle recharging stations. In a more remote perspective, also the use as on-board sources in electric vehicles has been envisaged [6]. The present technological issues on VRFBs include system scale-up and optimization for large industrial applications capable of improved performances and reduced costs, in order to foster their competitiveness and diffusion [7]. Modeling and simulations are pivotal tools to obtain a comprehensive understanding of how the battery performance is affected by the design of felt, membranes, solution flow patterns, and operating procedures [8].

In this framework, thermal control is emerging as a critical issue in VRFB battery design [9]. In fact, the electrolyte temperature must be maintained within a given range (e.g. from –5°C to 50°C, in the case of 2.5 M vanadium solutions in sulfate-chloride mix) since low temperatures cause V^{2+} and V^{3+} precipitation [10], while VO_2^+ precipitates at high temperatures [11], [12], [13], [14]. This salt precipitation occurs according to the following irreversible reaction [15]

$$2VO_2^+ + H_2O \rightarrow V_2O_5 + 2H^+ \quad (1)$$

and can result in the occlusion of the cell flow channels, triggering major problems during battery operations or during stand-by period with pumps turned-off [16], [17], [1]. This problem could be addressed by lowering the vanadium ion concentration below 1.8 M, but this strategy reduces the already modest energy density [18]. Chemical stabilization of the vanadium species by means of

organic or inorganic additives [11] can only constitute a partial solution to prevent precipitation. In addition, high temperatures can enhance major side effects, such as hydrogen and oxygen evolution [19]. Recently, a strategy for improving the VRFB efficiency has been proposed [20], [21], that consists in reducing the reversible cell voltage during charge and increasing it during discharge by changing the electrolyte temperature. Thermal control has also been recommended in the integration of micro flow batteries with electronic devices, that could allow to cope with power supply demand and thermal management of printed boards for microelectronics used in high-performance servers [22], [23]. In addition, thermal analyses are important because a number of parameters which are crucial for a VRFB performance, e.g. electrolyte viscosity, cell internal resistance, and electrode potentials, depend on the electrolyte temperature. Analysis of these issues can profit remarkably by thermal numerical analyses. Thermal models can be important tools in the optimization of VRFB control procedures in standby and operating conditions. However, few thermal models have been reported in these two conditions. In [5] and [24] a two-dimensional model and a three-dimensional model, respectively, calculate the temperature distribution in the porous electrodes of a single cell, whereas [25] and [15] present a dynamic thermal model of a 2.5 kW/15kWh VRFB based on energy and mass conservation equations, though neglecting the reaction entropic heat [19]. The same research unit examined the effects of cell number, flow rate, tanks dimension and environmental temperature on the thermal behavior of a VRFB stack in load condition in [26] and modeled the shunt current effects on the battery temperature evolution in [27]. However, few experimental analyses on large stack have been documented [28] and no experimental validation of thermal models of industrial-scale VRFBs has yet been reported to our knowledge.

In this paper we present a cell-resolved dynamic model capable of simulating the temperature distribution in a VRFB stack in any operating conditions that takes into account the entropic heat, ions crossover and inherent side reactions, and shunt current losses. The model is based on energy and mass balance equations coupled with an equivalent circuit for computing the shunt currents. The losses in the circulating pumps are also included. The model has been validated against the

experimental data taken from a 9kW/27kWh VRFB test facility. An application of the model simulating the high-current (400-A) long-duration (8-h) operations of a large VRFB system is also presented. Important information was obtained about the electrolyte temperature evolution in next-generation industrial scale VRFB systems. The paper is organized as follows. The model is presented in Section 2. The test facility used for model validation is presented in Section 3 and the experimental validation in Section 4. Finally, the thermal simulation of a large VRFB is proposed in Section 5.

Nomenclature

Full symbols

A	membrane area
A_k	cross-sectional area in the k-th direction / of k-th element
C	vanadium concentration
C_p	specific heat at constant pressure
d	membrane thickness
E	voltage
E_a	activation energy
E_0	open circuit voltage (OCV)
E_0'	corrected standard potential = 1.37 V
F	Faraday constant = 96485 C mol^{-1}
I	current
j	j-th vanadium ions
K	universal gas constant = 8.314 J $K^{-1}mol^{-1}$
k	diffusivity coefficient
l	length
N	number of cells
P	power, heat rate
q	volumetric flow rate
R	electric resistance
SOC	state of charge
T	temperature
t	time
U	overall heat transfer coefficient
V	volume
V_c	cell volume
ρ	electrolyte density
α	electrolyte flow factor
ΔH	enthalpy change
ΔS	entropy change
σ	electrical conductivity

Subscripts

+	positive compartment
–	negative compartment

air	air
c	cell
ch	charge
co	crossover (irreversible)
di	discharge
end	end
fl	flux of electrolyte
sa	sulfuric acid
i	internal
j	*j*-th vanadium ions
il	irreversible losses (in load operation)
m	manifold
max	maximum
min	minimum
n	*n*-th cell
ip	inlet pipe (from tank to stack)
op	outlet pipe (from stack to tank)
pf	pumping friction
s	stack
re	reversible entropic
std	standard
t	tank
tr	transferred
x	*x* direction (axial, see Fig. 3)
y	*y* direction (transverse, see Fig. 3)
z	*z* direction (vertical, see Fig. 3)

2 Stack thermal model

The thermal model of the stack in load conditions takes into account the reversible entropic heat of the main reactions, the cell irreversible losses due to overpotentials, the self-discharge reactions due to species crossover and all the losses related to shunt currents. The mass balance equations and the thermal balance equations were coupled with the equations of an equivalent electrical circuit model. In order to take into account each cell thermal behavior, not only the heat exchanges of the stack, piping and tanks toward the surrounding air were considered, but also between adjacent cells. The following assumptions were adopted:

1) Each cell was assumed isothermal in its electrodes and membrane (i.e. as a continuous stirred tank reactor [5] and independent cell temperatures were considered.
2) After species crossover, self-discharge reactions were instantaneous;

3) No oxygen and hydrogen evolution occurred if the state of charge (*SOC*) was in the range from 0.05 to 0.95 [15];
4) The species conductivities were assumed constant with the temperature.

2.1 Electrochemical and chemical reactions

The main electrochemical reversible reactions occurring during a VRFB charge and discharge are:

$$VO^{2+} + H_2O \underset{di}{\overset{ch}{\rightleftarrows}} VO_2^+ + e^- + 2H^+, \quad E_0^+ = 1.0V\ (positive\ electrode) \tag{2}$$

$$V^{3+} + e^- \underset{di}{\overset{ch}{\rightleftarrows}} V^{2+}, \quad E_0^- = -0.26V\ \ (negative\ electrode) \tag{2}$$

In addition, due to species crossover through the membranes, exothermic side reactions take place, without electric energy conversion, which cause self-discharge and heat generation. As the negative-side species V^{3+} and V^{2+} diffuse through the membranes and enter the positive side, they react with VO^{2+} and VO_2^+ [16] [29]:

$$V^{2+} + 2VO_2^+ + 2H^+ \rightarrow 3VO^{2+} + H_2O \tag{3}$$

$$V^{3+} + VO_2^+ \rightarrow 2VO^{2+} \tag{4}$$

$$V^{2+} + VO^{2+} + 2H^+ \rightarrow 2V^{3+} + H_2O \tag{5}$$

Conversely, as the positive-side species VO^{2+} and VO_2^+ diffuse through the membranes and enter the negative side, they react with V^{3+} and V^{2+}:

$$VO^{2+} + V^{2+} + 2H^+ \rightarrow 2V^{3+} + H_2O \tag{6}$$

$$VO_2^+ + 2V^{2+} + 4H^+ \rightarrow 3V^{3+} + 2H_2O \quad (7)$$

$$VO_2^+ + V^{3+} \rightarrow 2VO^{2+} \quad (8)$$

The reactions (3) and (4) at the positive half-cells and (6) and (7) at the negative half-cells, which respectively involve the charged species VO_2^+ and V^{2+}, are the dominant effects as long as VO_2^+ is present at the positive half-cell and V^{2+} at the negative one, as happens in any load operation. Conversely, the reactions (5) and (8) can't occur as long as VO_2^+ or V^{2+} are present in the positive and negative half-cells, respectively, which is the case during load operation. Consequently, the reactions (5) and (8) have not been considered in the present model.

2.2 State of Charge

The state of charge is the ratio between the concentrations of the charged species and of all species in a compartment. Crossover causes different species concentrations in the two compartments resulting in two *SOCs*:

$$\begin{aligned} SOC_+ &= C_V/(C_V + C_{IV}) = C_V/C_+ \\ SOC_- &= C_{II}/(C_{II} + C_{III}) = C_{II}/C_- \end{aligned} \quad (9)$$

where C_j (with *j*=*II*, *III*, *IV*, *V*) is the concentration of the vanadium species *V*(*j*).

2.3 Shunt current computation

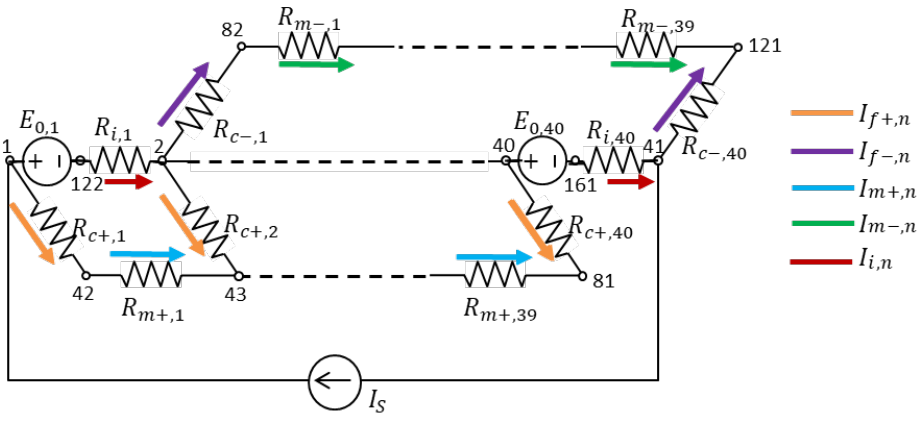

Fig. 1. Stack and cells equivalent electric network for shunt current computation [30].

Since the cells of a VRFB stack are connected in series, homologous (i.e. positive or negative) cell electrodes have different electric potentials. The hydraulic channels and manifold provide solutions in parallel to these electrodes, creating an electric path because the solutions are conductive. The electrical currents flowing in all these paths are known as "Shunt currents". At the aim of computing shunt currents, the stack was modeled as a lumped electric circuit (Fig. 1). Each cell was represented as a Thévenin equivalent made of a voltage source $E_{0,n}$ in series with a resistance $R_{i,n}$, with $n = 1, \dots N$ (N is the number of cells in the stack). Both these parameters are constant with the current but vary with the *SOC* and temperature T; $R_{i,n}$ also depends on the charge/discharge operation. $E_{o,n}$ corresponds to the cell open circuit voltage (*OCV*) and was computed with the Nernst equation expressed as a function of *SOCs*, based on (9):

$$E_0 = \left[\left(E_{0,+} - E_{0,-}\right) + \frac{2K\,T}{F} ln\, C_{H^+}\right] + \frac{K\,T}{F} ln\left(\frac{C_V}{C_{IV}}\frac{C_{II}}{C_{III}}\right) \quad (10)$$

$E_0' = \left[\left(E_{0,+} - E_{0,-}\right) + (2KT/F) ln\, C_{H^+}\right]$ is a corrected standard potential accounting for proton concentration effects [33]. K is the universal gas constant and F the Faraday constant. By expressing the concentrations C_j (j = *II*, *III*, *IV*, *V*) as functions of *SOCs* by means of eq. (9), eq. (10) was rewritten as:

$$E_0 = E_0' + \frac{K\,T}{F} ln \frac{SOC_+ SOC_-}{(1-SOC_+)(1-SOC_-)} \quad (11)$$

The internal resistance $R_{i,n}$ takes into account all cell overpotentials, which are typically dominated by the linear ohmic term. Fig 2 shows the values of $R_{i,n}$ as a function of the average *SOC* in charge and discharge, experimentally obtained from the test facility described in Section 3. These data show that $R_{i,n}$ is lower during charge, due to the different kinetics, being VO^{2+} oxidation faster than VO_2^+ reduction.

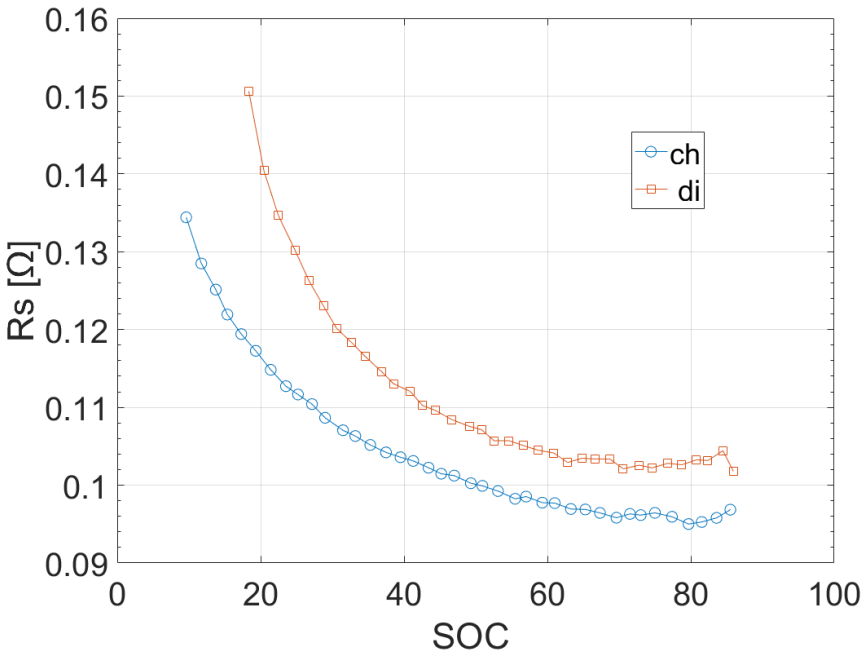

Fig. 2. IS-VRFB stack internal resistance profile vs. *SOC* during charge (*ch*) and discharge (*di*).

The resistances of the manifold and channel segments inside the stack were computed as:

$$R_{k\pm,n} = \frac{l_{k,n}}{\sigma_{\pm,n}\ A_{k,n}} \tag{12}$$

where l and A are the length and cross-sectional area of the segment; k is m for the manifold segment connecting two adjacent cells or c for the cell frame/plate channels (the latter term was added with the resistance of the cell felt flow field, computed by means a numerical analysis); +, – denote the positive and negative electrodes, respectively. The electric conductivities of the solutions, σ_+ and $\sigma\_$, were calculated as:

$$\sigma_+ = SOC_+\ \sigma_V + (1 - SOC_+)\ \sigma_{IV} \tag{13}$$

$$\sigma_- = SOC_-\ \sigma_{II} + (1 - SOC_-)\ \sigma_{III} \tag{14}$$

where σ_j (j = *II*, *III*, *IV*, *V*) denotes the vanadium ion conductivities, which were assumed to be constant with the temperature (Table 1). More details on the electric model are reported in [17], [30]. The model allowed to compute the shunt currents $I_{k\pm,n}$ in the circuit segments (i.e. in all resistances of Fig. 1) and the related Joule losses were obtained by multiplying these currents with the corresponding voltages in each segment.

2.4 Mass balance

In load condition, the species balance for the n-th cell depends on the cell current $I_{i,n}$, resulting from the stack current I_s and shunt currents $I_{c\pm,n}$, as well as on the species crossover and related side reactions (3), (4), (6), (7). By modeling the species crossover across the membrane with Fick's law, the mass balance equations for the negative compartment were written as:

$$\frac{V_c}{2}\frac{dC_{II-,n}}{dt} = -\left(k_{II,n}\,C_{II-,n} + 2k_{V,n}\,C_{V+,n} + k_{IV,n}\,C_{IV+,n}\right)\frac{A}{d} + \frac{1}{F}I_{i,n} + q_{c-}\left(C_{II-,t} - C_{II-,n}\right) \quad (15)$$

$$\frac{V_c}{2}\frac{dC_{III-,n}}{dt} = \left(-k_{III,n}C_{III-,n} + 3k_{V,n}\,C_{V+,n} + 2k_{IV,n}\,C_{IV+,n}\right)\frac{A}{d} - \frac{1}{F}I_{i,n} + q_{c-}\left(C_{III-,t} - C_{III-,n}\right) \quad (16)$$

$$\frac{V_c}{2}\frac{dC_{IV-,n}}{dt} = 0 \quad (17)$$

Similar equations were used for the positive compartment:

$$\frac{V_c}{2}\frac{dC_{V+,n}}{dt} = -\left(k_{V,n}C_{V+,n} + 2k_{II,n}C_{II-,n} + k_{III,n}C_{III-,n}\right)\frac{A}{d} + \frac{1}{F}I_{i,n} + q_{c+}\left(C_{V+,t} - C_{V+,n}\right) \quad (18)$$

$$\frac{V_c}{2}\frac{dC_{IV+,n}}{dt} = \left(-k_{IV,n}\,C_{VI+,n} + 3k_{II,n}\,C_{II-,n} + 2k_{III,n}\,C_{III-,n}\right)\frac{A}{d} - \frac{1}{F}I_{i,n} + q_{c+}\left(C_{IV+,t} - C_{IV+,n}\right) \quad (19)$$

$$\frac{V_c}{2}\frac{dC_{III+,n}}{dt} = 0 \quad (20)$$

In the previous equations, the diffusion coefficient of the j-th vanadium species (j = *II*, *III*, *IV*, *V*) in the n-th membrane was modeled with an Arrhenius-like dependence on temperature [15]:

$$k_{j,n} = k_j \, e^{-\frac{E_a}{K T_n}} \tag{21}$$

where k_j is a diffusivity reference value and E_a is the activation energy, that was assumed equal in all four vanadium ions (Table 1).

2.5 Heat generation

In load operation, the heat generation inside the stack is related to different factors, as presented hereafter.

a) The irreversible main heat rate P_{il} produced by the electric currents $I_{i,n}$ as stated in Section 2.2; it must be noted that this heat rate occurs by far inside the cells (where it consists of the overpotential losses represented by the internal resistances $R_{i,n}$) while the other hydraulic segments (represented by $R_{c,n}$ and $R_{m,n}$) produce negligible contributions.

b) The reversible entropic heat rate P_{re} released or absorbed inside the cells by the electrochemical reactions which generate the electric currents $I_{i,n}$ during discharge and charge, respectively [9].

c) The heat rate P_{co} due to exothermic self-discharge reactions (3), (4), (6) and (7) occurring after species crossover. The last two terms were computed as:

$$P_{re} = \frac{I_{i,n} \, T (\Delta S_- + \Delta S_+)}{F} \tag{22}$$

$$P_{co} = -\frac{A}{d}\left(k_{II,n} C_{II-,n} \, \Delta H_2 + k_{III,n} C_{III-,n} \Delta H_3 + k_{IV,n} \, C_{IV+,n} \Delta H_4 + k_{V,n} C_{V+,n} \Delta H_5\right) \tag{23}$$

In eq. (22), $\Delta S_+ = (S_{VO^{2+}} + S_{H_2O} - S_{VO_2^+})$ and $\Delta S_- = (S_{V^{3+}} - S_{V^{2+}})$ are the entropy changes of discharge reactions in the positive and negative half-cell, respectively. Since the entropy values could be deduced from [27] and [31] only at standard temperature T_{Std} = 298,15 K (Table

1), the values in eq. (22) were considered constant with T. In eq. (23), ΔH_2, ΔH_3, ΔH_4, and ΔH_5 are the enthalpy changes of the exothermic side reactions (3), (4), (6), (7).

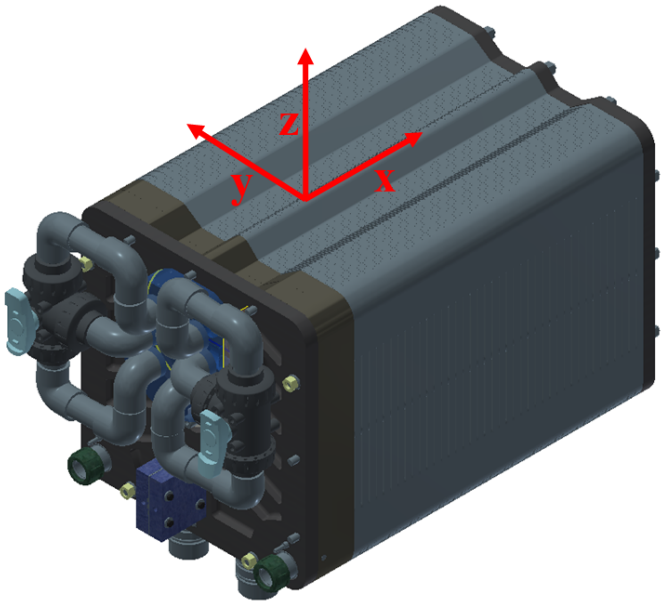

Fig. 3. IS-VRFB stack, consisting of N=40 cell with interposed bipolar plates. The x, y, and z directions are represented.

2.6 Energy balance

The temperature of each cell was computed by taking into account its thermal balance equation:

$$\rho C_p V_C \frac{dT_n}{dt} = P_{il} + P_{re} + P_{co} + P_{tr} + P_{fl} \quad (24)$$

where the last two terms express the heat exchanges as described hereafter. The heat transfer (both conductive and convective) of the *n-th* cell (except the end ones) toward the other cells and the surrounding air, was computed as:

$$P_{tr} = U_x A_x (T_{n+1} - T_n) + U_x A_x (T_{n-1} - T_n) + 2U_y A_y (T_{air} - T_n) + 2U_z A_z (T_{air} - T_n) \quad (25)$$

The convective heat transfer coefficients in the *x*, *y*, and *z* directions U_x, U_y, and U_z (Fig. 3) were computed as reported in a previous work [17].

The equations for the first and last cells had to take into account that one face in *x* direction exchanges with the surrounding air so that the pertinent term of eq. (25) was replaced with $U_{end}A_{end}(T_{air} - T_1)$ and $U_{end}A_{end}(T_{air} - T_N)$, respectively. The heat exchange due to the electrolyte flow in each cell was obtained as:

$$P_{fl} = \rho C_p q_{c+}\left(T_{ip+} - T_n\right) + \rho C_p q_{c-}\left(T_{ip-} - T_n\right) \tag{26}$$

The heat dissipation of the piping and tanks were computed considering their outer surfaces subject to natural convection. As regards the internal surfaces, forced convection was assumed in the pipes due to the high solution velocity, and natural convention in the tanks.

The heat exchanged by the positive electrolyte along the two pipe segments connecting the tank to the stack and the stack back to the tank, were written respectively as:

$$\rho C_p V_{ip} \frac{dT_{ip+}}{dt} = \rho C_p q_{s+}\left(T_{t+} - T_{ip+}\right) + U_{ip}A_{ip}\left(T_{air} - T_{ip+}\right) + P_{pf} \tag{27}$$

$$\rho C_p V_{op} \frac{dT_{op+}}{dt} = \rho C_p q_{s+}\left(T_{op+} - T_{t+}\right) + U_{op}A_{op}\left(T_{air} - T_{op+}\right) \tag{28}$$

where the subscripts have the following meanings: *ip* = inlet pipe segment from tank to stack, *op* = outlet pipe segment from stack to tank; *t* = tank. P_{pf} is the pump heating from hydraulic friction, given in the pump data sheet (Fig. 4). The other symbols in eq. (27) and (28) are explained in Table 1.

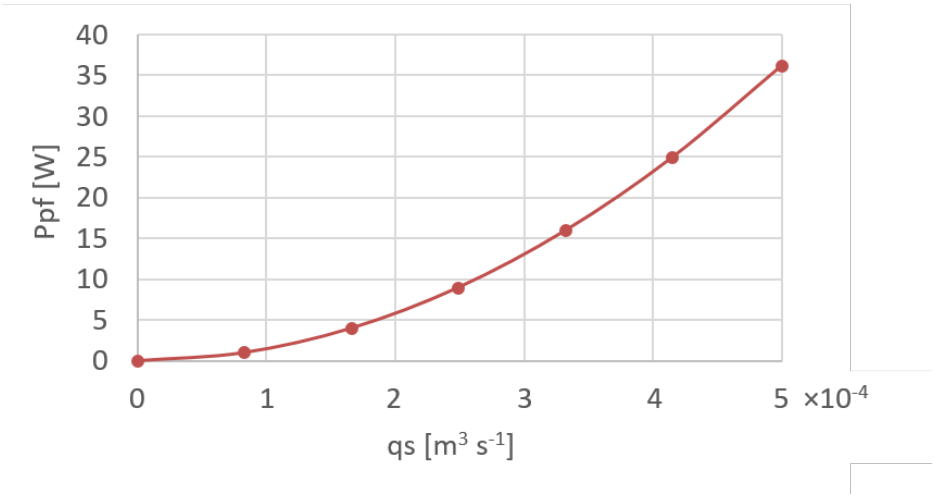

Fig. 4. Energy losses of the pumps (SANSO PMD-641) as a function of flow rate

The thermal equation of the electrolyte in the positive tank was written as:

$$\rho C_p V_t \frac{dT_{t+}}{dt} = \rho C_p q_{s+}\left(T_{op+} - T_{t+}\right) + U_t A_t\left(T_{air} - T_{t+}\right) \tag{29}$$

Equations similar to (27), (28), and (29) hold for the piping and tank at the negative side.

3 IS-VRFB experiment

The model was validated against data measured on the industrial-scale VRFB (IS-VRFB) test facility that is in operation at the Electrochemical Energy Storage and Conversion Laboratory of the University of Padua. Its stack consists of N = 40 cells with active area A = 600 cm^2 and has been tested with currents up to 400 A and powers up to 9 kW. Each tank contains 550 L of 1.6 M vanadium in 4.5 M sulfuric acid solution corresponding to a capacity of 27 kWh [32]. The IS-VRFB parameters and the physical constants used in the simulations are shown in Table 1.

Table 1
Parameters and physical constants used in the simulations

Symbols	Parameters	Values
A	Membrane active area	0.06 m^2
A_x	Cell heat transfer area in x direction	0.06 m^2
A_y	Cell heat transfer area in y direction	1.648 ×10^{-3} m^2
A_z	Cell heat transfer area in z direction	2.416 ×10^{-3} m^2
C	Total vanadium concentration	1600 mol m^{-3}
C_p	Electrolyte specific heat capacity	3200 J kg^{-1}K^{-1}

C_{sa}	Sulfuric acid concentration	4500 mol m^{-3}
d	Membrane thickness	50 μm
E_a	Activation energy of the electrolytes	17340 J mol^{-1}
k_{II}	Reference diffusivity of V^{2+} in Nafion 212 [33]	5.76 ×10^{-3} $cm^2 min^{-1}$
k_{III}	Reference diffusivity of V^{3+} in Nafion 212 [33]	2.1 ×10^{-3} $cm^2 min^{-1}$
k_{IV}	Reference diffusivity of VO^{2+} in Nafion 212 [33]	6.26 ×10^{-3} $cm^2 min^{-1}$
k_V	Reference diffusivity of VO_2^+ in Nafion 212 [33]	3.84 ×10^{-3} $cm^2 min^{-1}$
N	Number of cells in the stack	40
U_{end}	Overall end cell heat transfer coefficient in *x* direction [17]	2.877 $Wm^{-2}K^{-1}$
U_{ip}	Overall heat transfer coefficient of inlet piping [16]	3.667 W $m^{-2}K^{-1}$
U_{op}	Overall heat transfer coefficient of outlet piping [16]	3.667 W $m^{-2}K^{-1}$
U_t	Overall tank heat transfer coefficient [16]	5.73 4 W $m^{-2}K^{-1}$
U_x	Overall cell heat transfer coefficient in *x* direction [17]	21.67 W $m^{-2}K^{-1}$
U_y	Overall cell heat transfer coefficient in *y* direction [17]	2.413 W $m^{-2}K^{-1}$
U_z	Overall cell heat transfer coefficient in *z* direction [17]	1.376 W $m^{-2}K^{-1}$
V_C	Cell electrolyte volume	0.4968 ×10^{-3} m^3
V_{ip}	Volume of piping from stack outlet to tank	2.2 ×10^{-3} m^3
V_{ip}	Volume of piping from tank to stack inlet	2.2 ×10^{-3} m^3
V_t	Tank volume	0.5 m^3
ΔH_2	Enthalpy of reaction in eq. (3) [16]	–220 kJ mol^{-1}
ΔH_3	Enthalpy of reaction in eq. (4) [16]	–64 kJ mol^{-1}
ΔH_4	Enthalpy of reaction in eq. (6) [16]	–91.2 kJ mol^{-1}
ΔH_5	Enthalpy of reaction in eq. (7) [16]	–246.8 kJ mol^{-1}
ΔS_+	Entropy change of discharge reaction at positive electr. [27] [31]	–0.0884 kJ $mol^{-1}K^{-1}$
ΔS_-	Entropy change of discharge reaction at negative electr. [27] [31]	–0.0379 kJ $mol^{-1}K^{-1}$
ρ	Electrolyte density	1354 kg m^{-3}
σ_{II}	Conductivity of V^{2+}	27.5 S m^{-1}
σ_{III}	Conductivity of V^{3+}	17.5 S m^{-1}
σ_{IV}	Conductivity of VO^{2+}	27.5 S m^{-1}
σ_V	Conductivity of VO_2^+	41.3 S m^{-1}

In IS-VRFB, the electrodes, membrane and flat bipolar plates forming the cells are assembled into polypropylene frames and the stack end plates are of stainless steel. Each hydraulic circuit is provided with a centrifugal pump (PMD-641 by SANSO, Japan) driven by an inverter that allows an accurate control of the flow rates. The pipes connecting the tanks to the stack of the positive and negative compartments have the same length and internal volume. Two electromagnetic flowmeters (Proline Promag by Endress+Hauser, Switzerland) provide volumetric flow-rate measurements to an accuracy of ±0.5% while two differential pressure gauges (Deltabar PMD by Endress+Hauser) measure the solutions pressure drops in the stack to a precision of ±450 Pa. Four Pt-100 temperature probes (TR11 by Endress+Hauser) provide measurements of the solutions temperatures at each

stack inlet and outlet to an accuracy of ±0.15 K. A further Pt-100 sensor is used to measure the room air temperature. The battery charge and discharge are controlled by a power management system (PMS), which consists of a remotely controlled two-quadrant static converter. A customized system supervisor, i.e. the battery management system (BMS), has been built around a Labview environment with hardware made of a desktop computer and a National Instruments (NI, US) compact data acquisition (Compact DAQ) interface, which allow data management and experiment control.

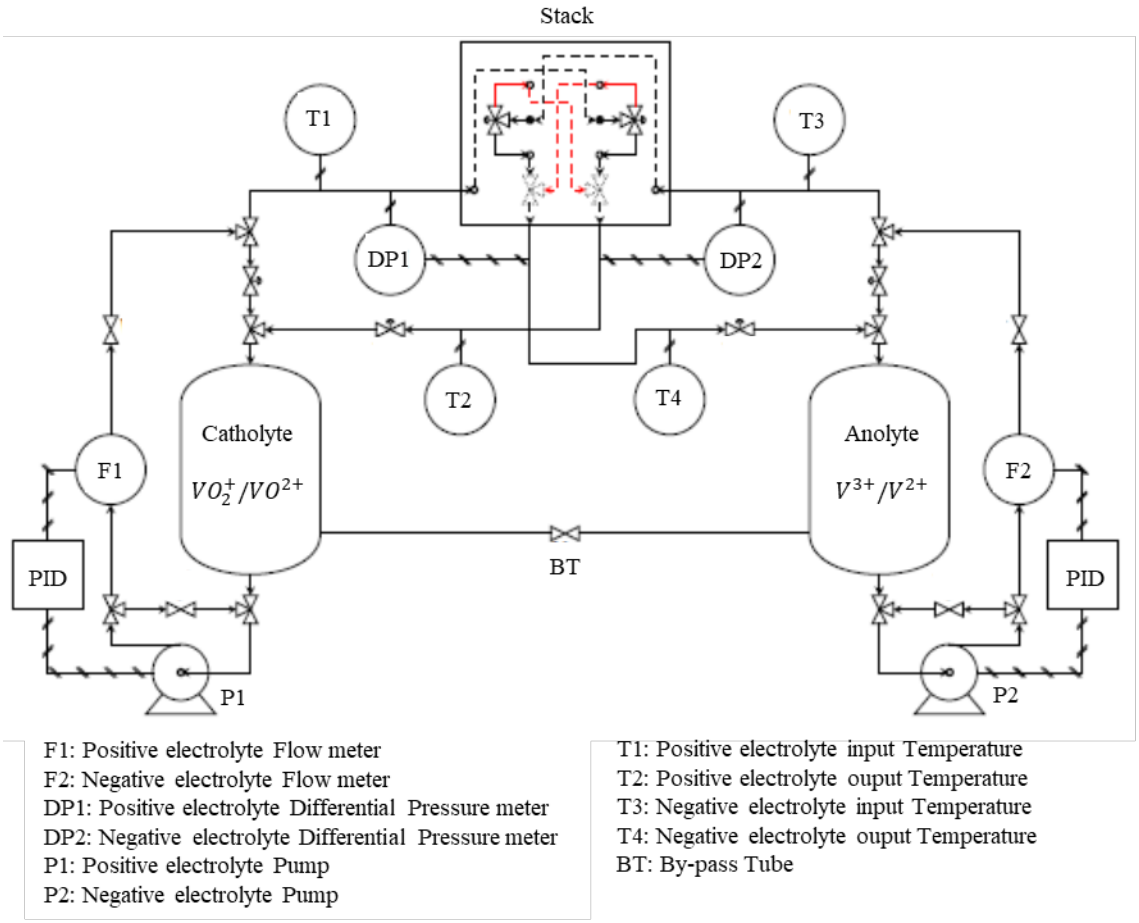

Fig. 5. Scheme of the IS-VRFB test facility

4 Experimental validation

The dynamic thermal model was validated against experimental data taken from the IS-VRFB test facility, operated in discharge and charge at a stack current I = 70 A and with solution flow rates

$q_{s+} = q_{s-} = 30$ L min^{-1} (i.e. a specific flow rate $q_s/NA = 20.8 \cdot 10^{-3}$ cm s^{-1}) for 2.25 hours. Correspondingly, the battery was discharged from *SOC* = 0.78 to 0.35 and charged from *SOC* = 0.08 to 0.50. The duration of each test was 2 h and 15 min. To ensure that the ambient condition was almost the same, tests were started at the same time (9:00 a.m.) in two consecutive days. The temperatures at the stack inlet and outlet, provided by the four sensors T1 … T4 (Fig. 5) were recorded every 0.8 seconds. An additional Pt-100 sensor monitored the air temperature, that was about 24 °C at the test start and gradually increased by 2 °C during both the tests. All simulations were carried out using the parameters listed in Table 1 and, based on the actual experimental conditions, the initial temperature in the tanks and stack was set at 32 °C in discharge and at 29.4 °C in charge.

The validations in both charge and discharge were performed by comparing T1 with T_{ip+} and T2 with T_{op+} as regards the positive side and T3 with T_{ip-} and T4 with T_{op-} as regard the negative side. Fig. 6 shows the evolutions of the measured and computed electrolyte temperatures at these positions.

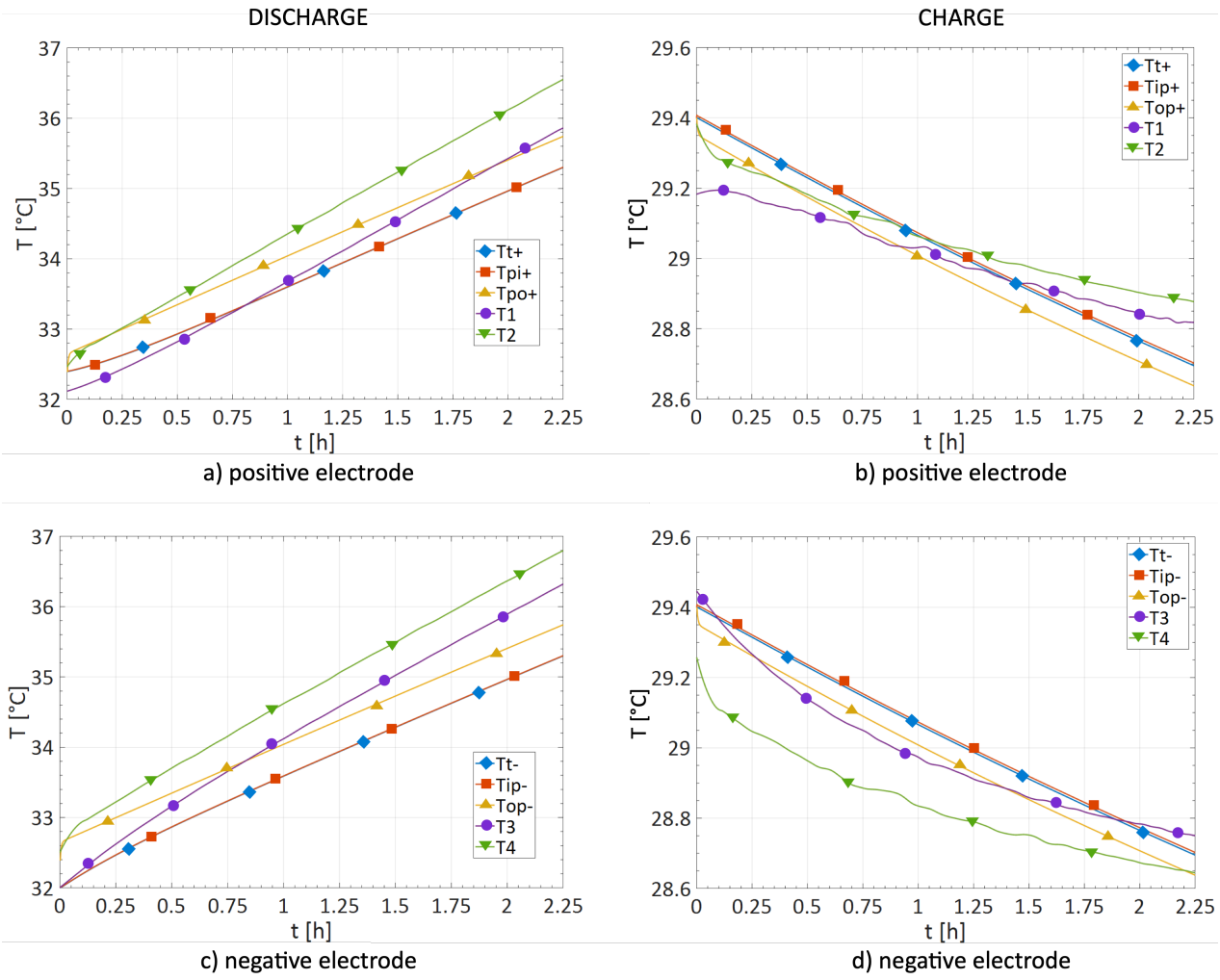

Fig.6. Computed and measured electrolyte temperature evolutions at the inlet and outlet pipes during charge and discharge. $T_{t+/-}$= computed electrolyte temperatures in the positive/negative tank; $T_{ip+/-}$= computed electrolyte temperatures in the positive/negative input pipes; $T_{op+/-}$= computed electrolyte temperatures in the positive/negative output pipes; $T_{1/3}$= measured electrolyte temperatures in the positive/negative input pipes; $T_{2/4}$= measured electrolyte temperatures in the positive/negative output pipes.

During discharge (Fig. 6 a) and c)), simulated and measured temperatures present a maximum discrepancy of 0.9°C, as a result of the assumed simplifications and the uncertainty of some thermal coefficients taken from the literature. Such a small discrepancy indicates that the model is able to simulate properly the temperature rise in the electrolytes. The comparison between simulated and measured temperatures during charge (Fig. 6 b) and d)) shows a lower maximum discrepancy, below

0.2°C, indicating that in this phase the model reproduces even better the temperature decrease in both electrolytes, at the limit of instrument accuracy.

The temperature increases during discharge and decrease during charge, because of the different effect of P_{il} and P_{re}: while the former is always positive, the latter is positive during discharge (being the reactions exothermic) and negative during charge (being the reactions endothermic), with $P_{il} < |P_{re}|$. In both cases, P_{co} is much lower than the previous two heat rates.

Under the assumptions of Section 2 and with the parameters used in the model, the computed temperatures of the positive and negative solutions are the same: the small discrepancies between the numerical results and the measured values show that the model was appropriate to simulate the thermal behavior of the system during both charge and discharge processes.

5 High-current simulations of a large VRFB

The model was applied to investigate the thermal behavior of an industrialized VRFB unit under heavy operating conditions. The study assumed the same stack as in IS-VRFB, but working at 400 A (i.e. at current density above 650 mA cm^{-2}) with a flow rate q_s = 30 L min^{-1} for the positive and negative electrolytes (this performance has been actually achieved in IS-VRFB with a cell voltage of 0,45 V [34]). The study was intended to investigate the battery thermal behavior over a working period as long as 8 hours both in charge and discharge; a proper tank capacity was considered at this aim. In particular, the assumed flow rate, that is quite low for the given current, imposed a *SOC* in a narrow range, in order to assure an adequate reactant flow, even considering a flow factor (i.e. ratio of flux of ions provided by the electrolyte flow with respect to the generated electric current) as low as α_{min} = 2. The maximum *SOC* during charge and the minimum *SOC* in discharge, both reached after 8 h of operation, were:

$$SOC_{ch,max} = 1 - \frac{N\ I\ \alpha_{\min}}{F\ C\ q_s} \qquad \text{charge} \tag{30}$$

$$SOC_{di,min} = \frac{I\ N\ \alpha_{min}}{F\ C\ q_s} \qquad \text{discharge} \tag{31}$$

Consequently, the *SOC* could be varied in the range 0.05–0.59 during charge and in the range 0.95–0.41 during discharge. To this aim, a capacity of 5000 L for each tank was assumed, with an energy capacity of 240 kWh.

Consequently, the pipe lengths and tank surfaces were assumed tenfold larger than those of IS-VRFB, while the thermal parameters of pipes and tanks were given the values of Table 1. During both charge and discharge, the air temperature was set at 20°C, namely at a value compatible with an installation in an air-conditioned room or container. The initial solution temperature in the tanks and stack was set at 32 °C, as resulting from some previous operation.

Fig. 7 a) and b) show the stack reversible entropic heat rate P_{re} in load operations: it is positive (since the reactions are exothermic) during discharge and negative (endothermic reactions) during charge [17]. In both operations the P_{re} values are almost constant and the very small variations shown in the figures are due to secondary effects.

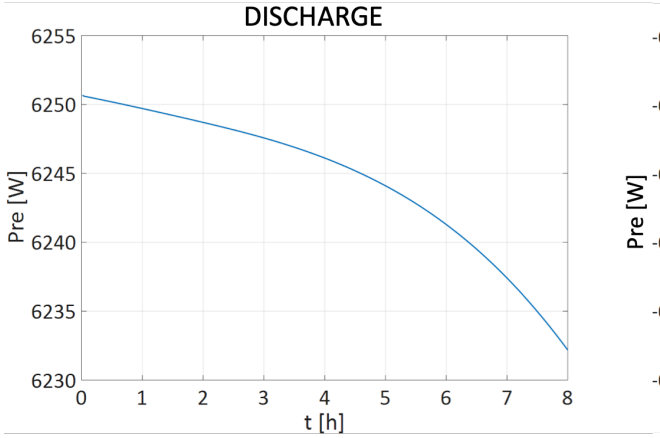

a) reversible entropic heat rate

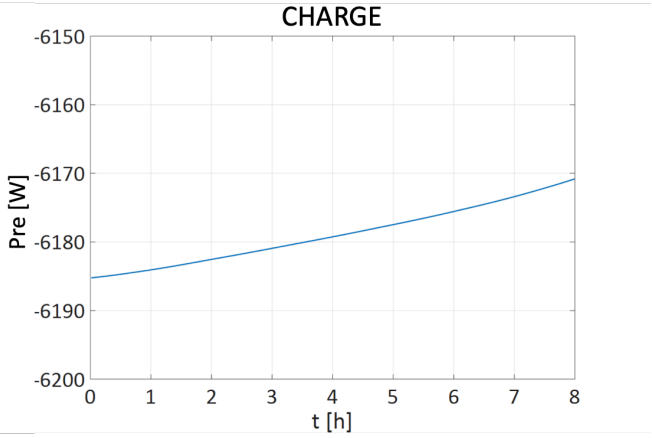

b) reversible entropic heat rate

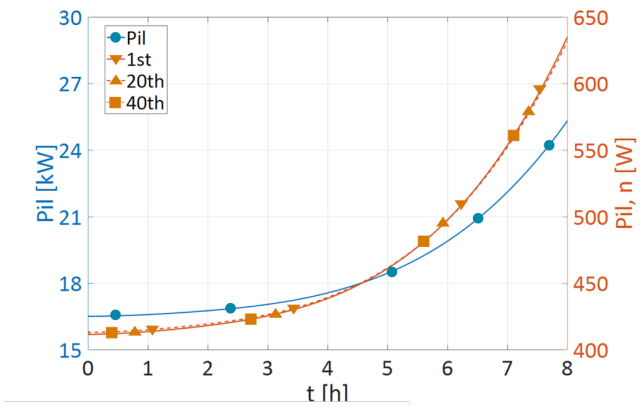

c) main irreversible heat rate: *il,n*=cell; *il*=total

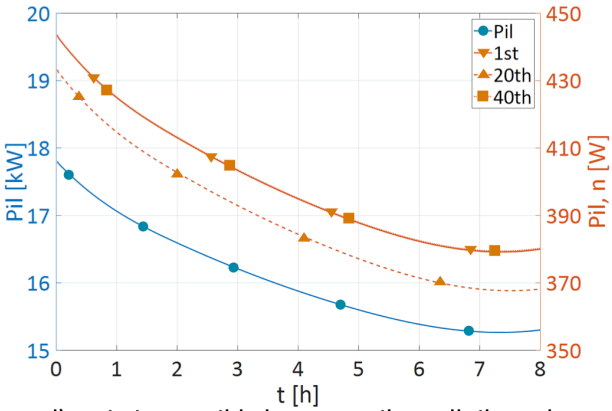

d) main irreversible heat rate: *il,n*=cell; *il*=total

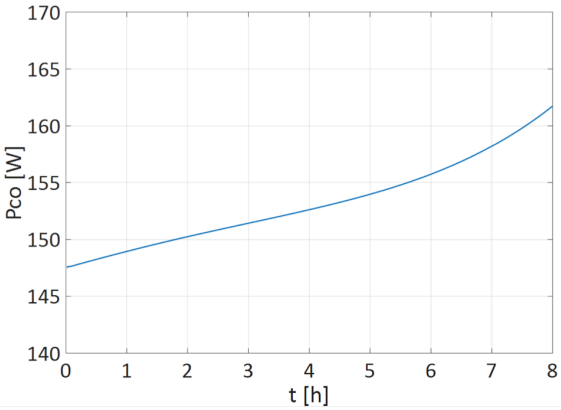

e) crossover heat rate

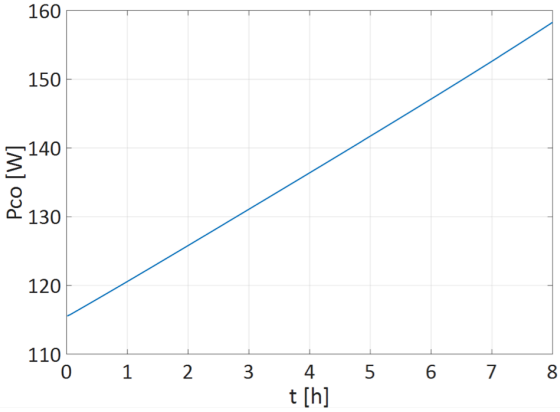

f) crossover heat rate

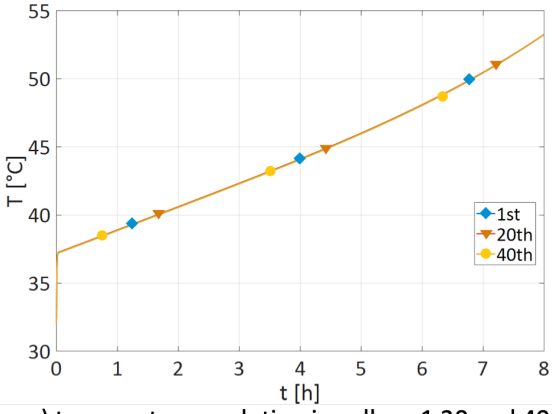

g) temperature evolution in cells *n*=1,20 and 40

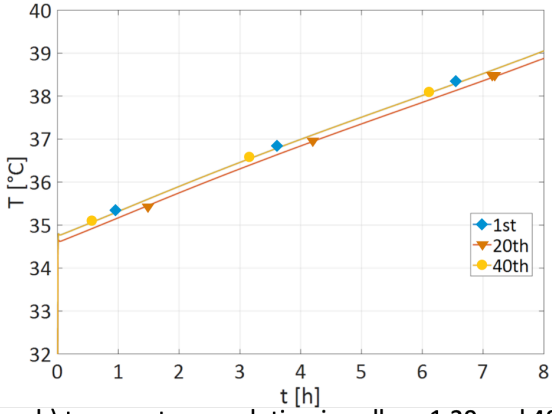

h) temperature evolution in cells *n*=1,20 and 40

Fig. 7. Simulation of high-current (400 A) long-duration (8 hours) discharge and charge: heat rate contributions and electrolyte temperature in cells # 1, 20 and 40.

Fig. 7 c) and d) show the stack irreversible heat rate P_{il} together with the contribution in three cells $P_{il,n}$ with n = 1, 20 and 40 (the last one) in both discharge and charge. In agreement with the internal resistance profiles of Fig. 2, these heat rates increase with decreasing *SOC* during discharge and decrease with increasing *SOC* during charge. During discharge (Fig 7 c), the cell contributions $P_{il,n}$ are almost equal. In fact, different $P_{il,n}$ values could arise from different values of the shunt currents in the hydraulic segments [17] [30], but in the discharge conditions here studied, shunt currents are much lower than the stack current I_s, so that all cells present almost the same current $I_{i,n} \cong I_s$. During charge (Fig. 7 d) some small differences between $P_{il,n}$, lower than 1%, appear because shunt currents are larger than in discharge, due the higher stack voltage.

Fig. 7 e) and f) show the crossover heat rate P_{co} in both discharge and charge: in both cases it increases as a consequence of the species diffusivity dependence on the increasing temperature. However, P_{co} is two orders of magnitude lower than P_{il} so that it is negligible in the overall thermal balances.

Fig.7 g) and h) presents the resulting temperature evolution in the three cells n = 1, 20 and 40. During discharge (Fig. 7 g), there is no evident difference between the cells, as a consequence of the heat generation discussed above. In addition, it can be noted that most of the heat is removed equally from all cells by the solution circulation, i.e. by P_{fl}, conversely than in stand by condition with pumps turned-off [17], thus enhancing the cell temperature equalization. During charge (Fig.7 h), that requires higher stack voltages, a marginal difference in the cell temperatures appears, as consequence of the slightly different released heat rates described above.

During discharge, all the heat rates have positive values, concurring to produce a temperature rise of 16°C in 8 hours of operation and the temperature rises more than linearly, due to the increasing values of P_{il} and $P_{il,n}$.

During charge, P_{il} is positive whereas P_{re} is negative, producing counteracting thermal effects. Since $P_{il} > |P_{re}|$, a net heat generation occurs, resulting in a temperature rise of 6°C in an 8-hour charge, smaller than during discharge over the same period of time, when both P_{il} and P_{re} are positive. It should be noted that when smaller load currents are applied, e.g. 70 A as in the validation simulations, $P_{il} < |P_{re}|$ can occur during charge, because the former term roughly scales with the square of the current while the latter is directly proportional to the current, so that a temperature decrease occurs, as shown in Fig. 6 b) and d). Operations at very high currents present major thermal issues also because of this effect.

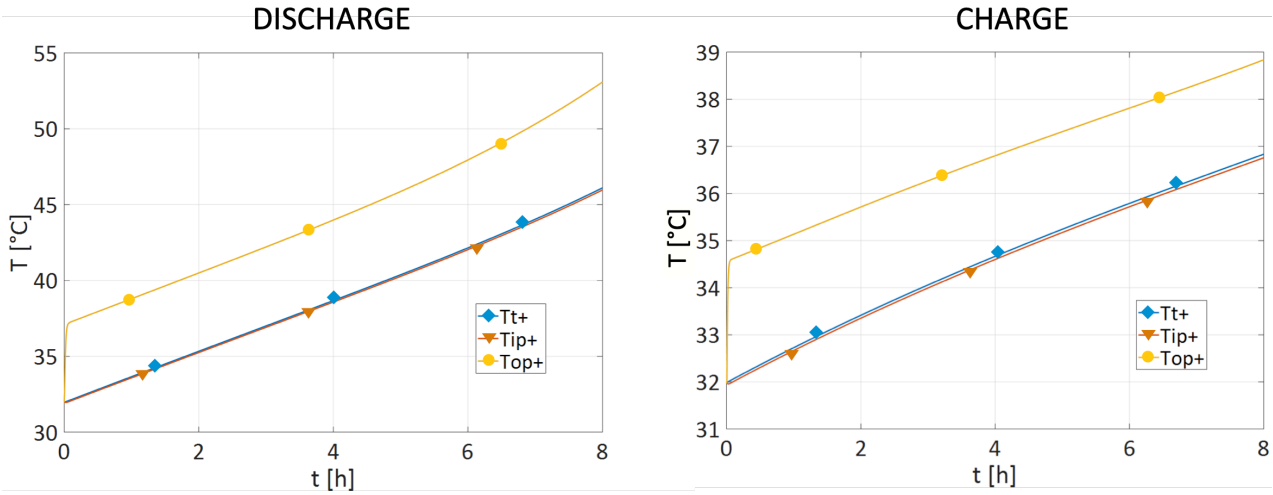

Fig. 8. Simulation of high-current (400 A) long-duration (8 hours) discharge and charge: positive electrolyte temperature at stack inlet (*ip*) and outlet (*op*) piping, and in the tank (*t*) (negative electrolyte has a similar evolution.)

Finally, Fig. 8 a) show the temperature evolution of the electrolytes during an 8 hour discharge in some points of the hydraulic circuits. The same profiles apply for the positive and negative compartments since the model does not account for differences between the two solutions, as already stated. The temperatures at the tank and stack inlet increase of 13°C in 8 hours, while the temperatures at the stack outlet rise by 21°C, due to the combined effects of the reaction reversible entropic heat and irreversible internal losses. The maximum electrolyte temperature after 8 hours exceeds 50°C, which can cause precipitation of VO_2^+ in the stack and tank. Therefore, when a VRFB

is operated at high current density as in these simulations, an electrolyte cooling system is needed in order to prevent such side effect.

Fig. 8 b) shows the temperature evolution of the electrolytes during an 8-hour charge. Also in this case, all temperatures increase, but at a smaller extent, consistently with the behaviors presented in Fig 7. A maximum temperature below 40 °C is reached, which is not critical for VO_2^+ precipitation. Due to the reduction of the irreversible heat with increasing *SOC* (i.e. of the internal resistance of Fig. 2) during charge, the temperature slope reduces during the process.

It is worth noticing that this simulation did not account for a heat exchanger specifically designed for the battery thermal management. Such a component can enhance the heat transfer and reduce the rise temperatures in the solutions so as to prevent species precipitation, in addition to optimize the battery performance. Moreover, since the irreversible heat P_{il} plays the major role in the heat generation at high current density, a strategy aimed at reducing the internal losses (i.e. the internal resistances $R_{i,n}$ of Fig. 1) is crucial not only in order to maximize a VRFB efficiency as reported in another paper [35], but also to control the thermal behavior and minimize the risk of VO_2^+ precipitation.

6 Conclusion

A complete dynamic thermal model of a VRFB under load conditions, namely in charge and discharge, based on the thermal dynamics of each cell was developed. The model evaluated the heat due to the reversible and irreversible effects, which occur inside the cells and the stack, including main electrochemical reactions, overpotentials, shunt currents, and species crossover with consequent self-discharge reactions. The crossover diffusion coefficients were considered temperature dependent, while the solution conductivities took into account the state of charge. In order to compute shunt currents and related losses in the cells and hydraulic segments, an equivalent electric circuit was implemented. It includes the cell equivalent internal resistances, which take into

account the overpotential effects and were measured experimentally. Shunt current losses occurring in the flow channel and manifold were evaluated and resulted negligible from the thermal point of view. The heat released by the losses of circulation pumps was also taken into account.

The model was validated against the measurements from a 9kW/27kWh VRFB test facility, showing that it is suitable to simulate the thermal behavior of an industrialized VRFB system during charge and discharge. More simulations were developed on a possible larger industrialized VRFB provided with the same stack and capable of discharging at 400 A (i.e. at current density above 650 mA cm^{-2}) through discharge/charge duration of 8 hours, in order to reproduce a real thermal stress condition. This long duration was intended to consider a major advantage of the VRFB technology, i.e. the independent sizing of power and energy that can be exploited to ensure long discharges. The simulations aimed to investigate critical thermal conditions, which may occur in a big plant installed in an air-conditioned container for grid services such as peak shaving.

The reversible heat associated with the main half-reactions has alternating thermal effects, being exothermic during discharge and endothermic during charge, which constitutes an advantage on other kind of batteries. As a consequence, the simulations showed the maximum temperatures at the end of a discharge phase. In the case of the high-current long-duration operation, a top temperature above 50°C was reached, which constitute an issue for the positive electrolyte thermal stability. In fact, when working at the high current densities, as expected from next-generation industrial VRFBs, the generated irreversible heat can exceed the absolute value of the reversible heat, because the former contribution roughly scales with the square of the stack current and the latter is directly proportional to the stack current.

Consequently, when operating at high current, the temperatures rise during both charge and discharge, calling for efficient cooling system in order to prevent species precipitation at high temperature. Even if the highest temperatures occur at the end of a discharge phase, when the concentration of VO_2^+ is low, VO_2^+ precipitation could represent an issue resulting in the occlusion of the small flow channels in the cell frames and battery faults. It can been concluded that the next

generation VRFBs, capable of higher power densities and high current densities, require specific heat exchanger to thermally assist the VRFB operation.

7 Acknowledgment

This work was funded by the University of Padua under the strategic project MAESTRA 2011 "From Materials for Membrane-Electrode Assemblies to Electric Energy Conversion and Storage Device" (cod. STPD11XNRY 002) and the Project 2016 of the Interdepartmental Centre Giorgio Levi Cases for Energy Economics and Technology "Next-Generation VRFB Energy Storage Systems" (GUAR_RICERCALASCITOLEVI17_02).

References

[1] Rychcik M, Skyllas-Kazacos M Characteristics of a new all-vanadium redox flow battery. J Power Sources 1988; 22: 59-67; doi:10.1016/0378-7753(88)80005-3.

[2] Kear G, Shah AA, Walsh FC. Development of the all-vanadium redox flow battery for energy storage: A review of technological, Financial and policy aspects. Int J Energy Res 2012; 36: 1105-1120; doi:10.1002/er.1863.

[3] Alotto P, Guarnieri M, Moro F. Redox flow batteries for the storage of renewable energy: A review. Renew Sustain Energy Rev 2014; 29: 325-335; doi:10.1016/j.rser.2013.08.001.

[4] Leung P, Li X, Ponce De León C, Berlouis L, Low CTJ, Walsh FC. Progress in redox flow batteries, remaining challenges and their applications in energy storage. RSC Adv 2012; 2: 10125-10156 doi:10.1039/c2ra21342g.

[5] Shah AA, Walsh FC. Electrochimica Acta Non-isothermal modelling of the all-vanadium redox flow battery. Electrochim Acta 2009; 55: 78–89; doi:10.1016/j.electacta.2009.08.009.

[6] Mohamed MR, Sharkh SM, Walsh FC. Redox flow batteries for hybrid electric vehicles: Progress and challenges. 5th IEEE Veh. Power Propuls. Conf. VPPC '09, 2009; 978: 4244-2601; doi:10.1109/VPPC.2009.5289801.

[7] Oh K, Yoo H, Ko J, Won S, Ju H. Three-dimensional, transient, nonisothermal model of all-vanadium redox flow batteries. Energy 2015; 81: 3-14; doi:10.1016/j.energy.2014.05.020.

[8] Guarnieri M, Mattavelli P, Petrone G, Spagnuolo G. Vanadium redox flow batteries: Potentials and challenges of an emerging storage technology. IEEE Ind Electron Mag 2016; 10: 20-31; doi:10.1109/MIE.2016.2611760.

[9] Xiong B, Zhao J, Tseng KJ, Skyllas-Kazacos M, Lim TM, Zhang Y. Thermal hydraulic behavior and efficiency analysis of an all-vanadium redox flow battery. J Power Sources 2013; 242: 314–324. doi:10.1016/j.jpowsour.2013.05.092.

[10] Kazacos M, Cheng M, Skyllas-Kazacos M. Vanadium redox cell electrolyte optimization studies. J Appl Electrochem 1990; 20: 463-467; doi:10.1007/BF01076057.

[11] Wang K, Zhang Y, Liu L, Xi J, Wu Z, Qiu X. Broad temperature adaptability of vanadium redox flow battery-Part 3: The effects of total vanadium concentration and sulfuric acid concentration. Electrochim Acta 2018; 259: 11–19; doi:10.1016/j.electacta.2017.10.148.

[12] Skyllas-Kazacos M, Cao L, Kazacos M, Kausar N, Mousa A. Vanadium Electrolyte Studies for the Vanadium Redox Battery-A Review. ChemSusChem 2016; 9: 1521-1543; doi:10.1002/cssc.201600102.

[13] Oboroceanu D, Quill N, Lenihan C, Eidhin DN, Albu SP, Lynch RP, et al. Effects of Temperature and Composition on Catholyte Stability in Vanadium Flow Batteries: Measurement and Modeling. J Electrochem Soc 2017; 164: A2101–A2109; doi:10.1149/2.1401709jes.

[14] M. Skyllas-Kazacos, C. Menictas MK. Thermal stability of concentrated V(V) electrolytes in the vanadium redox cell. J Electrochem Soc 1996; 143: L86-L88; doi:10.1149/1.1836609.

[15] Tang A, Bao J, Skyllas-Kazacos M. Thermal modelling of battery configuration and self-discharge reactions in vanadium redox flow battery. J Power Sources 2012; 216: 489-501; doi:10.1016/j.jpowsour.2012.06.052.

[16] Yan Y, Li Y, Skyllas-Kazacos M, Bao J. Modelling and simulation of thermal behaviour of

vanadium redox flow battery. J Power Sources 2016; 322: 116-126; doi:10.1016/j.jpowsour.2016.05.011.

[17] Trovò A, Marini G, Sutto G, Alotto, P, Giomo M, Moro F, Guarnieri M. Standby thermal model of a vanadium redox flow battery stack with crossover and shunt-current effects. Appl Energy 2019; 240; 893-906; doi.org/10.1016/j.apenergy.2019.02.067.

[18] Wei Z, Zhao J, Skyllas-Kazacos M, Xiong B. Dynamic thermal-hydraulic modeling and stack flow pattern analysis for all-vanadium redox flow battery. J Power Sources 2014; 260: 89–99; doi:10.1016/j.jpowsour.2014.02.108.

[19] Zhang C, Zhao TS, Xu Q, An L, Zhao G. Effects of operating temperature on the performance of vanadium redox flow batteries. Appl Energy 2015; 155: 349–353; doi:10.1016/j.apenergy.2015.06.002.

[20] Lee SW, Yang Y, Lee HW, Ghasemi H, Kraemer D, Chen G, et al. An electrochemical system for efficiently harvesting low-grade heat energy. 3942 Nat Commun 2014. doi:10.1038/ncomms4942.

[21] Reynard D, Dennison CR, Battistel A, Girault HH. Efficiency improvement of an all-vanadium redox flow battery by harvesting low-grade heat. J Power Sources 2018; 390: 30-37; doi:10.1016/j.jpowsour.2018.03.074.

[22] Marschewski J, Brenner L, Ebejer N, Ruch P, Michel B, Poulikakos D. 3D-printed fluidic networks for high-power-density heat-managing miniaturized redox flow batteries. Energy Environ Sci 2017; 10: 780-787; doi:10.1039/c6ee03192g.

[23] Andreev AA, Sridhar A, Sabry MM, Zapater M, Ruch P, Michel B, et al. PowerCool: Simulation of cooling and powering of 3D MPSoCs with integrated flow cell arrays. IEEE Trans Comput 2018. 67: 73-85; doi:10.1109/TC.2017.2695179.

[24] Ma X, Zhang H, Xing F. A three-dimensional model for negative half cell of the vanadium redox flow battery. Electrochim Acta 2011; 58: 238–246; doi:10.1016/j.electacta.2011.09.042.

[25] Tang A, Ting S, Bao J, Skyllas-Kazacos M. Thermal modelling and simulation of the all-vanadium redox flow battery. J Power Sources 2012; 203: 165–176; doi:10.1016/j.jpowsour.2011.11.079.

[26] Yan Y, Skyllas-Kazacos M, Bao J. Effects of battery design, environmental temperature and electrolyte flowrate on thermal behaviour of a vanadium redox flow battery in different applications. J Energy Storage 2017; 11: 104–118; doi:10.1016/j.est.2017.01.007.

[27] Tang A, McCann J, Bao J, Skyllas-Kazacos M. Investigation of the effect of shunt current on battery efficiency and stack temperature in vanadium redox flow battery. J Power Sources 2013; 242: 349–356; doi:10.1016/j.jpowsour.2013.05.079.

[28] Mohamed MR, Leung PK, Sulaiman MH. Performance characterization of a vanadium redox flow battery at different operating parameters under a standardized test-bed system. Appl Energy 2015; 137: 402–412; doi:10.1016/j.apenergy.2014.10.042.

[29] Li Y, Skyllas-Kazacos M, Bao J. A dynamic plug flow reactor model for a vanadium redox flow battery cell. J Power Sources 2016; 311: 57–67; doi:10.1016/j.jpowsour.2016.02.018.

[30] Moro F, Trovò A, Bortolin S, Del Col D, Guarnieri M. An alternative low-loss stack topology for vanadium redox flow battery: Comparative assessment. J Power Sources 2017; 340: 229–241; doi:10.1016/j.jpowsour.2016.11.042.

[31] Bard AJ, Faulkner LR. Electrochemical Methods Fundamentals and Applications-2nd ed. John Wiley, Inc 2001. doi:10.1016/B978-0-12-381373-2.00056-9.

[32] Guarnieri M, Trovò A, D'Anzi A, Alotto P. Developing vanadium redox flow technology on a 9-kW 26-kWh industrial scale test facility: Design review and early experiments. Appl Energy 2018; 230: 1425-1434; doi:10.1016/j.apenergy.2018.09.021.

[33] Tang A, Bao J, Skyllas-Kazacos M. Thermal modelling of battery configuration and self-discharge reactions in vanadium redox flow battery. J Power Sources 2012; 216: 489–501; doi:10.1016/j.jpowsour.2012.06.052.

[34] Trovò A, Marini G, Sutto A, Alotto P, Guarnieri M. High current polarization tests on a 9 kW Vanadium Redox Flow Battery stack. J Power Sources (Submitted).

[35] Maggiolo D, Zanini F, Picano F, Trovò A, Carmignato S, Guarnieri M. Particle based method and X-ray computed tomography for pore-scale flow characterization in VRFB electrodes. Energy Storage Materials 2019; 16: 91-96, doi: 10.1016/j.ensm.2018.04.021.